Available online at www.sciencedirect.com
ScienceDirect
Journal of Power Sources 162 (2006) 1312–1321
JOURNAL OF POWER SOURCES
www.elsevier.com/locate/jpowsour

Metal oxyfluorides $TiOF_2$ and NbO_2F as anodes for Li-ion batteries

M.V. Reddy [a], S. Madhavi [b], G.V. Subba Rao [a], B.V.R. Chowdari [a,*]

[a] *Department of Physics, National University of Singapore, Singapore 117542, Singapore*
[b] *School of Materials Engineering, Nanyang Technological University, Singapore 639798, Singapore*

Received 13 May 2006; accepted 15 August 2006
Available online 10 October 2006

Abstract

Lithium insertion and extraction in to/from the oxyfluorides $TiOF_2$ and NbO_2F is investigated by galvanostatic cycling, cyclic voltammetry and impedance spectroscopy in cells using Li-metal as a counter electrode at ambient temperature. The host compounds are prepared by low-temperature reaction and characterized by powder X-ray diffraction (XRD), Rietveld refinement and Brunauer, Emmett and Teller (BET) surface area. Crystal structure destruction occurs during the first-discharge reaction with Li at voltages below 0.8–0.9 V for Li_xTiOF_2 as shown by ex situ XRD and at ≤1.4 V for Li_xNbO_2F to form amorphous composites, 'Li_xTi/NbO_y–LiF'. Galvanostatic discharge–charge cycling of 'Li_xTiO_y' in the range 0.005–3.0 V at a current density of 65 mA g^{-1} gives a capacity of 400 (±5) mAh g^{-1} during 5–100 cycles with no noticeable capacity fading. This value corresponds to 1.52 mol of recycleable Li/Ti. The coulombic efficiency (η) is >98%. Results on 'Li_xNbO_y' show good reversibility of the electrode and a η >98% is achieved only after 10 cycles (range 0.005–3.0 V and at 30 mA g^{-1}) and a capacity of 180 (±5) mAh g^{-1} (0.97 mol of Li/Nb) was stable up to 40 cycles. In both 'Li_xTiO_y' and 'Li_xNbO_y', the average discharge and charge voltages are 1.2–1.4 and 1.7–1.8 V, respectively. The impedance spectral data measured during the first cycle and after selected numbers of cycles are fitted to an equivalent circuit and the roles played by the relevant parameters as a function of cycle number are discussed.

Keywords: Coulombic efficiency; Metal oxyfluorides; Anodes; Li-ion batteries; Capacity; Discharge–charge cycling

1. Introduction

Lithium-ion batteries (LIBs) are favoured for present day portable power sources for electronic applications due to their high specific energy, good rechargeability and safety in operation. Commercial LIBs employ a mixed oxide, namely, $LiCoO_2$, as the positive (cathode) electrode and graphite as the negative (anode) electrode material. During operation, the Li-ions intercalate/de-intercalate into/out of the electrodes and contribute to the capacity [1–3]. To reduce the cost, improve the capacity and safety-in-operation, efforts are being made to find alternative electrode materials for LIBs. Research on anode materials is concentrating on three types; as follows: (i) oxides that can intercalate- and de-intercalate Li-ions into the layered (2D) or network (3D) structure at low voltages versus Li-metal, e.g., $Li_4Ti_5O_{12}$ that possesses a cubic spinel structure [4–6]. (ii) Tin (Sn) metal or binary and ternary amorphous and crystalline Sn-oxides, which can form an alloy with Li ($Li_{4.4}Sn$) at $V < 0.5$ V versus Li and the capacity arises from the reversible alloying–de-alloying reaction [7–11]. (iii) Transition metal binary/ternary oxides that are reduced, at low voltages versus Li, to the respective nano-size metal (M) or metal-oxides containing M in a low-oxidation state. Under these conditions, the nano-size M or M_xO_y can catalytically decompose the lithium oxide, Li_2O to Li and contribute to the reversible capacity [12–17]; examples are shown in Eqs. (1) and (2) and are essentially displacement reactions:

$$CoO + 2Li^+ + 2e^- \leftrightarrow Co(nano) + Li_2O, \quad (1)$$

$$M_mO_{y+n} + 2yLi^+ + 2ye^- \leftrightarrow M_mO_n + yLi_2O \quad (M = Mo, V). \quad (2)$$

Studies have shown that in the case of both Sn- and M-oxides, the first-discharge reaction with Li-metal involves crystal structure destruction followed by the formation of Sn or M or M_mO_n in a matrix of Li_2O and any other metal/non-metal ion (M′) that acts as the matrix or 'spectator' element [15–17]. The starting

* Corresponding author. Tel.: +65 65162956; fax: +65 67776126.
E-mail address: phychowd@nus.edu.sg (B.V.R. Chowdari).

0378-7753/$ – see front matter © 2006 Elsevier B.V. All rights reserved.
doi:10.1016/j.jpowsour.2006.08.020

crystal structure (even though it is destroyed during the first discharge) and the nature and content of the matrix element appear to play a significant role in determining the stability and long-term cycleability of the Sn-oxides with Li [18–20]. Our investigations on oxides of the type $CaSnO_3$ [21], Ca_2SnO_4 [22] have shown that a perovskite structure consisting of corner-linked SnO_6 octahedra and Ca ions are a favourable structure and matrix element, respectively, in governing Li recycleability. A cubic structure with isolated SnO_6 octahedra and pyrophosphate (P_2O_7) groups as the matrix as in SnP_2O_7 was shown to be beneficial for the Sn compounds [19].

The metal oxyfluorides $TiOF_2$ [23] and NbO_2F [23,24] are iso-structural with the cubic ReO_3 and WO_3 phases. The crystal structures are built up of corner-sharing Ti(or Nb)X_6 (X = O, F) octahedra, where the X ions are randomly distributed. The 12-fold O-coordinated site, which can accommodate other ions, is empty. Since Ti and Nb ions are chemically reducible, Li-ions can be inserted into the vacant sites. Indeed, chemical insertion of Li using *n*-butyl lithium (*n*-BuLi) into $TiOF_2$ [25] and NbO_2F [25,26] has been reported years ago. Bohnke et al. [27,28] examined the electrochemistry of Li intercalation/de-intercalation into NbO_2F in the voltage range 0.5–3.5 V. Presently, we have investigated the electrochemical behaviour of $TiOF_2$ and NbO_2F with Li-metal under deep discharge–charge conditions (range 0.005–3.0 V). The results showed that the Li–$TiOF_2$ system exhibits a reversible capacity of 400 mAh g^{-1} without any noticeable capacity fading up to 100 cycles corresponding to ~1.5 mol of recycleable Li per mole of $TiOF_2$. The Li–NbO_2F system shows a lower reversible capacity, viz., 180 mAh g^{-1} (~1 mol of Li), but is stable up to 40 cycles.

2. Experimental

2.1. Preparation and characterization

$TiOF_2$ and NbO_2F in 5 g batches were prepared by the method reported by Permer and Lundberg [26]. High purity niobium/titanium metal powder (Merck) was treated with a 1:1 mixture of HF (aq.) (Merck, 48%) and HNO_3 (aq.) (J.B. Baker, 48%) and stirred for 24 h in a Teflon beaker. Slow evaporation (60–70 °C, 2 days) of the resulting clear solution to dryness using a hot plate yielded the respective crystalline metal oxyfluoride. Powder X-ray diffraction (XRD) patterns of the compounds were recorded by means of Siemens D5005 unit with Cu Kα radiation in the step-scanning mode in the 2θ range of 20–140° at intervals of 0.02°, with a step time of 14 s. Rietveld analysis was carried out using TOPAS R (Version 2.1) software. The crystallographic model used for $TiOF_2$ was that reported by Vorres and Donohue [23], and for NbO_2F that reported by Carlson et al. [24]. For each refinement, the background parameter, scale factor, cell parameters, zero-point correction, atom positions, site-occupancy factors, isotropic thermal parameters and sample displacement were refined. The Brunauer, Emmett and Teller (BET) surface area of the powder was measured with a Micromeritics Tristar 3000 (USA).

2.2. Electrochemical characterization

The electrodes were fabricated using Ti/Nb oxyflouride as the active material, super P carbon black (ENSACO) and Kynar 2801 as the binder in a weight ratio of 80:10:10. The mixture was dissolved in *N*-methyl pyrrolidone (NMP, Merck) solvent to form a uniform viscous slurry by stirring. The slurry was coated on to a copper foil by the doctor-blade technique and then dried in an air oven at 80 °C for 24 h. The foil was pressed between twin rollers, cut into 16 mm diameter circular strips, and finally dried in a vacuum oven at 70 °C for 12 h. The active material in the electrode was about 6–8 mg and the geometrical area of the electrode was 2.0 cm^2. Coin-type test cells (size 2016) were assembled using the electrode with the active material, Li-metal foil (16 mm diameter; 0.595 mm thick, Kyokuto Metal Co. Ltd., Japan) as the counter and reference electrodes, a 1 M solution of $LiPF_6$ in ethylene carbonate (EC) and diethyl carbonate (DEC) (1:1, v/v; Merck) as the electrolyte and polypropylene separator (Celgard) in an argon-filled glove box (MBraun, Germany). Details of the cell fabrication have been described earlier [29,30]. Charge–discharge cycling and cyclic voltammetry were carried out at ambient temperature (25 °C) by using a multichannel battery tester (Model SCN, Bitrode, USA) and a Macpile II System (Biologic, France). Ex situ XRD of the cycled electrodes was carried out as follows: several cells were fabricated with $TiOF_2$ electrodes and aged for 24 h. They were discharged to the desired voltage at 30 mA g^{-1} and held for 3 h. One cell was discharged to 0.005 V and then charged to 3.0 V. The cells were dismantled in the glove box, the electrode was recovered along with the Cu-foil, washed with anhydrous DEC to remove the $LiPF_6$ salt from the electrode, dried and then mounted on the XRD holder (Al-metal) along with protective adhesive tape. A computer controlled Solartron impedance/gain-phase analyzer (Model SI 1255) coupled to a battery test unit (Model 1470) was used for conducting impedance measurements on cells at room temperature. The frequency range was from 0.35 MHz to 3 mHz with an ac signal amplitude of 5 mV. Data were analyzed using *Z* plot and Z view software (Version 2.2, Scribner Associates Inc., USA) to obtain the Nyquist plots.

3. Results and discussion

3.1. Structural aspects

The $TiOF_2$ and NbO_2F oxyfluorides are white crystalline solids and quite stable towards exposure to air and moisture. As pointed out by Permer and Lundberg [26], the synthesis of NbO_2F and $TiOF_2$ by the present method under 'mild' conditions not only yields a crystalline product without any further heat treatment but is also 'anhydrous'. On the other hand, when Nb_2O_5 is used as the starting material instead of Nb powder, the acid salt $NbO_2F{\cdot}HF$ always forms and has to be heated at high temperature (>500 °C) to remove the HF and obtain the pure oxyfluoride. The powder XRD patterns of the oxyfluorides show them to be pure with diffraction lines characteristic of cubic symmetry. Rietveld refined powder X-ray diffraction profiles of NbO_2F and $TiOF_2$ are shown in Fig. 1. Both the oxyfluorides

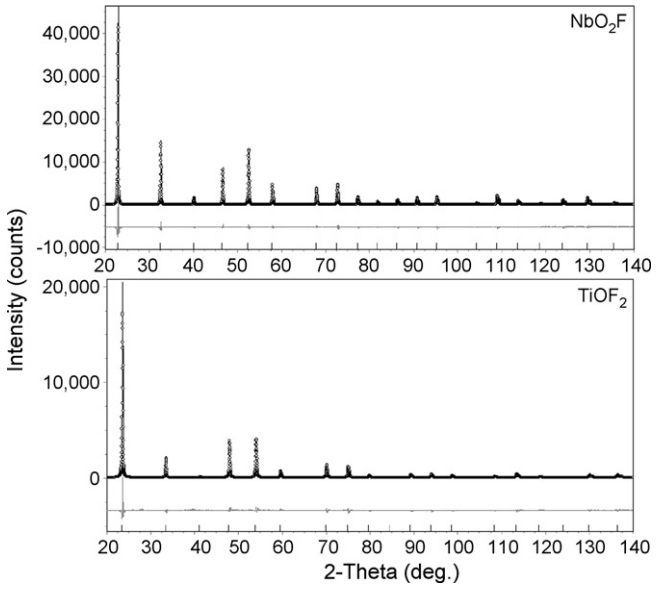

Fig. 1. Rietveld refined X-ray diffraction profile (experimental, calculated and difference) of NbO_2F and $TiOF_2$ with respective Bragg reflection markers. Experimental data are shown as continuous line and the simulated pattern as overlapped circles. The lower trace is the difference between calculated and experimental intensities. Cu Kα radiation.

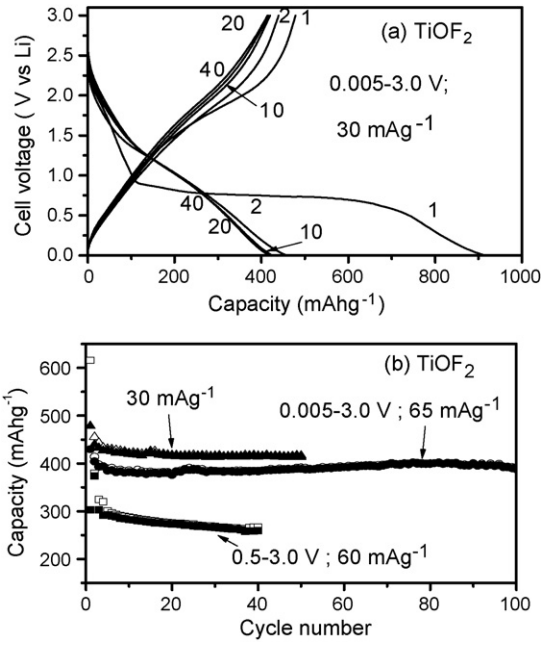

Fig. 2. (a) Galvanostatic charge–discharge curves of $TiOF_2$ in voltage range 0.005–3.0 V vs. Li at 30 mA g^{-1}. The cycle number is indicated. (b) Capacity vs. cycle number for $TiOF_2$. Voltage ranges and specific current are indicated. Filled and open symbols represent discharge and charge capacity, respectively.

belong to the cubic *Pm3m* space group with an *a* lattice parameter of 3.9059(2) Å for NbO_2F and 3.8019(4) Å for $TiOF_2$. The crystal sizes obtained from Rietveld refinement of the XRD patterns are 139 (±5) nm for NbO_2F and 88 (±5) nm for $TiOF_2$. The (*x*, *y*, *z*) and occupancy parameters used for the Rietveld refinement for $TiOF_2$ are: Ti(0, 0, 0), 1.0; O(0, 0, 0.5), 0.33; F(0, 0, 0.5), 0.67. The respective values for NbO_2F are: Nb(0, 0, 0), 1.0; O(0.5, 0, 0), 0.65; F(0.5, 0, 0), 0.35. The *R* Bragg factor for the NbO_2F refined pattern is 4.9 and that of $TiOF_2$ is 5.2, which are reasonably good values. The above *a* values are in good agreement with those reported for $TiOF_2$ ($a = 3.798$ Å) [25] and NbO_2F ($a = 3.902$ Å) [25,26]. The measured BET surface areas of $TiOF_2$ and NbO_2F are small, namely, 0.27 and 0.40 (±0.02) $m^2\ g^{-1}$, respectively, despite the low temperature used for the synthesis.

3.2. Charge–discharge cycling of $TiOF_2$ and NbO_2F

Galvanostatic charge–discharge curves have been recorded in the voltage windows 0.005–3.0, 0.5–3.0 and 1.0–3.0 V versus Li at current densities ranging from 15 to 65 mA g^{-1} up to 100 cycles at room temperature. The open-circuit voltage (OCV) of the fabricated and aged (24 h) cells is about 2.8–3.0 V. The first discharge corresponds to the reaction of Li with $TiOF_2/NbO_2F$. The voltage versus capacity profiles of $TiOF_2$ up to 40 cycles are shown in Fig. 2a; for clarity only selected cycles are presented. During the first discharge, the voltage continuously decreases until a capacity of about 100 mAh g^{-1} is reached. Based on the weight of the active material in the composite electrode and the molar mass of $TiOF_2$, this corresponds to about 0.38 mol of Li consumed in a single-phase reaction, and is due to the insertion (intercalation) of Li in to the lattice (12-fold O-coordinated sites) without destroying the crystal structure. It is noted that this matches very well with $x = 0.35$ reported by Madhavi [29] and $x = 0.43$ by Murphy et al. [25] in Li_xTiOF_2 obtained with chemical intercalation using *n*-BuLi. In the discharge profile, a voltage plateau commences at about 0.85–0.9 V and continues up to about 750 mAh g^{-1} (~2.85 mol of Li/Ti). A plateau in the voltage–capacity profile is generally an indication of two different phases in equilibrium [12,13,16–19]. Accordingly, the plateau region in Fig. 2a (first cycle) can be assigned to the coexistence of Li_xTiOF_2 and Li_yTiOF_2 with $y > x$. Ex situ XRD, described below, reveals that the crystal structure is destroyed in the process and Li_yTiOF_2 is indeed an amorphous phase. After the plateau, the voltage of the cell decreases continuously until the lower cut-off voltage of 0.005 V with a capacity of 910 mAh g^{-1} (3.46 mol of Li/Ti) is reached. This additional consumption of 0.61 mol of Li occurs as a single-phase reaction that involves the amorphous matrix to give Li_zTiOF_2 or 'Li_zTiO' + LiF.

The first-charge curve is different from the first-discharge curve (Fig. 2a), which indicates that Li extraction from the amorphous phase is occurring by a different mechanism. The cell voltage continuously increases with a small plateau at about 1.75 V. The total first-charge capacity is 478 mAh g^{-1} (1.82 mol of Li/Ti). The irreversible capacity loss (ICL) during the first cycle is 1.64 mol of Li. Such large values of ICL have also been observed in several prospective LIB anode materials that have been studied, like pure and mixed oxides of tin, or those of transition metal (M = Fe, Co, Mo). The ICL is due to the contributions arising from: (i) the intrinsic nature of the material and kinetic limitations of the reverse reactions of Eqs. (1) and (2) which depend on the current density [15,16]; (ii) irreversible

consumption of Li for the formation of the solid electrolyte interphase (SEI) [12–17]; (iii) electrolyte decomposition followed by the formation of a 'polymeric film' covering the metal nano-sized particles, in the case of pure/mixed M-oxides under deep discharge conditions [12–16,31]. A similar argument applies to the case of Li-reaction with $TiOF_2$.

The second-discharge curve is qualitatively different from the first-discharge curve since Li-insertion is now occurring into an amorphous matrix, 'Li_yTiO': the voltage decreases continuously from the OCV with a small plateau at about 1.2 V (Fig. 2a). The second-discharge capacity is 440 mAh g^{-1} (1.67 mol of Li/Ti). During 2–10 cycles, the charge–discharge curves overlap, including the respective voltage plateaux. In the range 10–50 cycles, both the charge and discharge capacities stabilize at 425 (±5) mAh g^{-1} (1.62 mol of Li/Ti) at a current rate 30 mA g^{-1} without any noticeable capacity fading (Fig. 2a and b). Experiments at a higher current rate of 65 mA g^{-1} yield similar curves and, as expected, slightly lower capacities. As can be seen from Fig. 2b, a reversible and very stable capacity of 400 (±5) mAh g^{-1} is observed in the range 5–100 cycles (0.005–3.0 V). This value corresponds to 1.52 mol of recyclable Li per mole of $TiOF_2$. The current rate of 65 mA g^{-1} corresponds to the *C*/6 rate assuming $1C = 400$ mA g^{-1}. It is also clear from Fig. 2a and b that the charge and discharge capacities are almost identical for a given cycle number (after 10 cycles) and indicate that the coulombic efficiency (η) at both current rates (30 and 65 mA g^{-1}) is >98%.

Galvanostatic cycling with $TiOF_2$ was also carried out at 60 mA g^{-1} up to 40 cycles in the voltage range 0.5–3.0 V to assess the effect of increasing the lower cut-off voltage. The discharge capacity of 280 (±5) mAh g^{-1} on the 10th cycle is found to degrade by ∼10%, after 40 cycles. The η is about 96% (Fig. 2b). Thus, it is necessary to subject amorphous 'Li_zTiO' to deep cycling (0.005–3.0 V versus Li) to realize high reversible capacities.

To establish that crystal structure destruction has occurred during the first-discharge reaction, ex situ XRD patterns of the $TiOF_2$ electrode in the virgin state, after discharging to various voltages and after the completion of the first discharge–charge cycle (0.005–3.0 V) were recorded. These are shown in Fig. 3. The intensities of the (1 0 0), (1 1 0), (2 0 0), (2 1 0) and (2 2 0) lines in the XRD pattern at 1.2 V are significantly decreased compared with those for the virgin electrode. On the other hand, the original high-intensity (1 0 0) line is barely noticeable in the pattern at 0.75 V, but it is completely absent, along with the disappearance of other lines, in the patterns taken at 0.25 and 0.005 V (Fig. 3). Only lines due to the Cu-foil (current-collector) and the Al-metal (sample holder) are observed. Hence, crystal structure destruction and amorphisation of the $TiOF_2$ lattice starts at 0.75 V, which coincides with the voltage plateau seen in the galvanostatic voltage–capacity profile (Fig. 2a). The amorphisation appears to be complete at 0.25 V. The XRD pattern taken at the end of the first cycle (charged to 3.0 V) is almost identical to that taken at 0.005 V. This indicates that Li-extraction is occurring from an amorphous 'Li–Ti–O' or 'Li–Ti–O–F' matrix.

The first-discharge curve of NbO_2F from the OCV (2.9 V) to 0.005 V at 30 mA g^{-1} is shown in Fig. 4a. There is a small voltage plateau at 1.75 V (corresponding to a capacity of 75 mAh g^{-1}) with a shoulder at 1.9 V (25 mAh g^{-1}). These plateaux correspond to Li-insertion into NbO_2F and the coexistence of pure and intercalated phases, viz., Li_xNbO_2F with different values of *x*. Thereafter, a broad voltage plateau occurs at 1.4 V (180 mAh g^{-1}) followed by a continuous decrease in voltage to 0.005 V, with small voltage plateaux at 0.75 and 0.5 V. The general nature of the first-discharge profile agrees with that reported by Bohnke et al. [28], who attributed their

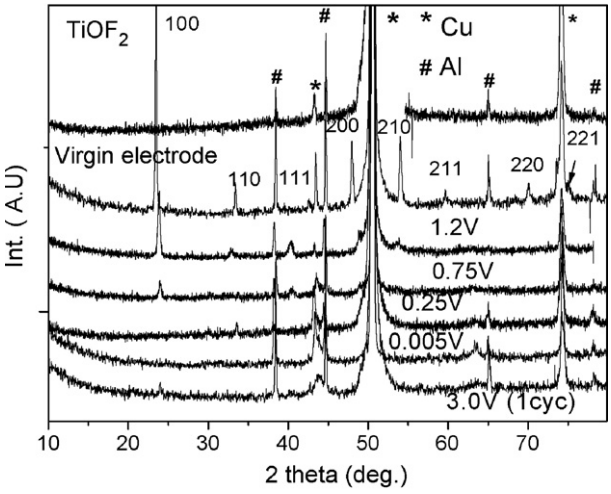

Fig. 3. XRD patterns of $TiOF_2$ composite electrode at various voltages during first discharge and at 3.0 V at the end of first cycle. The top pattern is that of etched Cu-foil. Miller indices of XRD peaks and voltages are shown. Symbols (*, #) represent Cu-metal and Al-metal (sample holder) lines. The *y*-axis values are normalized for all patterns except for the virgin electrode, Cu and Al-metals, to allow comparison after intercalation/de-intercalation.

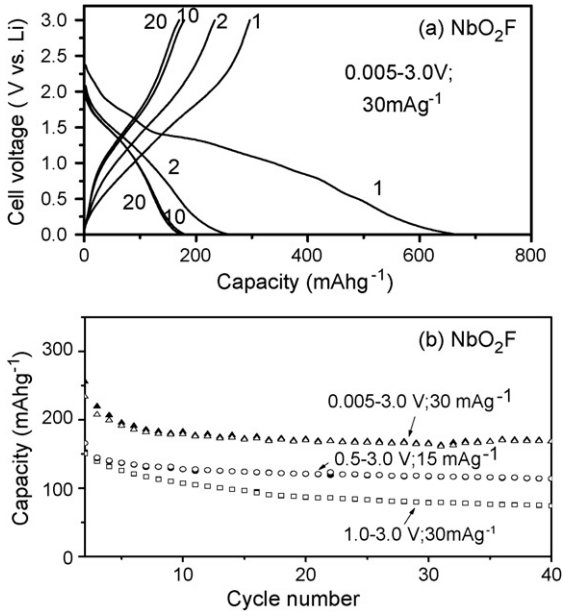

Fig. 4. (a) Galvanostatic charge–discharge curves of NbO_2F in voltage range 0.005–3.0 V vs. Li at 30 mA g^{-1}. The cycle number is indicated. (b) Capacity vs. cycle number for NbO_2F. Voltage ranges and specific current are indicated. Filled and open symbols represent discharge and charge capacity, respectively.

observed voltage plateaux at 1.9 and 1.75 V, to the co-existence of phases with $x = 0.15$ (α-phase) and 0.40 (β-phase), respectively. The broad voltage plateau at 1.4 V versus Li possibly signifies that further lithiation leads to destruction of the crystal structure, similar to the case of $TiOF_2$. Indeed, amorphisation of crystalline NbO_2F on deep discharge with Li, either chemically using *n*-BuLi [25,26] or electrochemically [28], has already been reported. The total first-discharge capacity observed is 660 mAh g^{-1} (3.55 mol of Li/Nb).

The first-charge (extraction of Li) profile is qualitatively different from that for the first discharge, and shows a smooth increase in voltage with a small plateau at 1.8–2.0 V (Fig. 4a). Thereafter, the voltage increases rapidly up to the upper cut-off of 3.0 V. The total first-charge capacity is 296 mAh g^{-1} (1.58 mol of Li/Nb). Thus, NbO_2F shows an ICL of 1.97 mol of Li during the first cycle, which is 0.33 mol larger than that found with $TiOF_2$. The second-discharge profile shows barely noticeable voltage plateaux at about 1.4 and 0.8–0.9 V and this indicates that Li-insertion is occurring in an amorphous matrix, 'Li–Nb–O–F'. The total Li-insertion capacity decreases significantly during second discharge, to 260 mAh g^{-1}. The second-charge profile follows an identical trend to that of the first-charge curve but shows some electrode polarization. Good reversibility of the electrode and a $\eta > 98\%$ is achieved only after 10 cycles. As can be seen from Fig. 4a and b, the 10th cycle capacity of 180 (±5) mAh g^{-1} (0.97 ± 0.03 mol of Li) is stable up to 40 cycles (0.005–3.0 V; 30 mA g^{-1}).

Cycling with the lower cut-off voltages of 0.5 or 1.0 V gives lower capacities and also leads to some capacity fading. Thus, in the range 0.5–3.0 V and at current rate of 15 mA g^{-1}, the third cycle capacity of 146 (±5) mAh g^{-1} degrades to 115 (±5) mAh g^{-1} after 40 cycles. In the voltage range 1.0–3.0 V and at 30 mA g^{-1}, the third cycle capacity of 138 mAh g^{-1} decreases to 76 (±5) mAh g^{-1} after 40 cycles (Fig. 4b). From Figs. 2a and 4a, it is noted that in both $TiOF_2$ and NbO_2F the average discharge voltage is 1.2–1.4 V and the average charge voltage is 1.7–1.8 V after the respective 10th cycle. These voltage values compare well with those found for other transition metal oxides such as CoO and NiO [3,12], $Ca_2Co_2O_5$ [31], $CaMoO_4$ [32], $CaWO_4$ [33] and in TiF_3 (1.0–1.2 V, discharge; 1.8–2.0 V, charge) [34].

3.3. Cyclic voltammetry

Cyclic voltammograms (CV) recorded on cells with $TiOF_2$ as cathode at room temperature in the range 0.005–3.0 V at a scan rate of 58 μV s^{-1} up to 15 cycles are shown in Fig. 5a. The counter and reference electrodes were Li-metal. Only select cycles are shown for clarity. The first sweep was taken towards negative potentials (reaction with Li) and started from the OCV, i.e., 2.9 V. As can be seen, a smooth sloping curve up to 0.8–0.9 V is indicative of single-phase insertion of Li and reduction of Ti^{4+} ions in $TiOF_2$ to form Li_xTiOF_2. This is followed by a large increase of $|i|$ (current) and a well-defined peak centred at 0.35 V, with a clear shoulder at 0.70–0.75 V. The latter coincides with the onset of a large voltage plateau region observed in the galvanostatic voltage–capacity profile (Fig. 2a) and indicates the beginning of a two-phase region. Thereafter, the $|i|$ decreases up to the lower cut-off potential, 0.005 V. The subsequent charge curve is smooth up to 1.5 V and exhibits a peak at 1.85 V, which coincides with the voltage plateau in the galvanostatic charging curve (Fig. 2a). The second cathodic sweep differs from the first, i.e., a broad cathodic peak at 1.8 V, a well-defined peak at 1.2 V and a minor peak at 0.5 V are seen. The as-mentioned peak is not seen in subsequent cathodic sweeps (6th and 15th cycle shown in Fig. 4a). The anodic peak at 1.8 V persists and good overlap of the voltammograms is evident from the sixth cycle onwards, which demonstrates the good reversibility of the Li–$TiOF_2$ system.

The CVs of NbO_2F versus Li up to 15 cycles are presented in Fig. 5b. The first cycle cathodic peak occurs at ∼2.15 V followed by another at ∼1.7 V, which represent the two-phase regions of NbO_2F and Li_xNbO_2F, with varying values of x (≤0.3). The distinct large intensity peak, which commences at 1.4 V and ends at 1.1 V, and the small intensity peaks at 0.75 and 0.40 V in the negative-going sweep are indicative of a two-phase equilibrium between the crystalline and/or amorphous phases with values of $x \geq 2$ in Li_xNbO_2F. These features have also been observed in the galvanostatic profile shown in Fig. 4a. The first-charge scan exhibits only a broad peak centred at 1.7–1.8 V and is due to extraction of Li from the amorphous phase at this voltage. As expected, the second negative-going scan is qualitatively different from the first and has a broad peak at 1.35–1.40 V. From

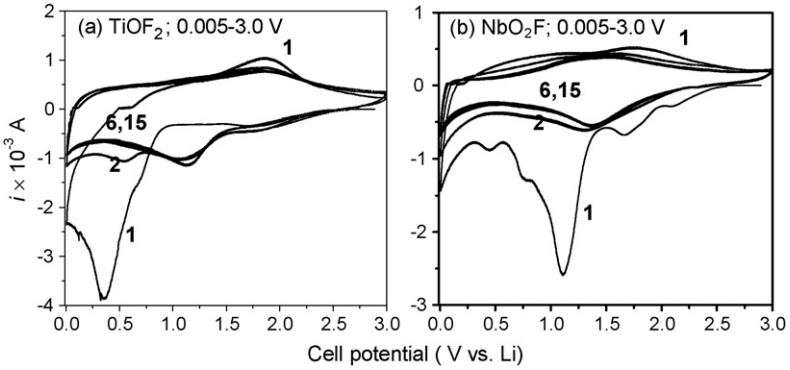

Fig. 5. Cyclic voltammograms of oxyfluorides. (a) $TiOF_2$ and (b) NbO_2F. Scan rate, 58 μV s^{-1}. Cycle number is indicated. Li-metal was used as the reference and counter electrodes. Voltage range is indicated.

the sixth cycle onwards, the voltammograms overlap well; each has only a single broad peak during the forward and backward scans and therefore confirms the reversibility of the Li–NbO_2F system. The general nature of the above CVs agrees with those reported by Bohnke et al. [28] on NbO_2F recorded at a higher scan rate of 1 mVs^{-1}.

From the CV data, it is clear that the main difference between the two oxyfluorides is that Li^+ intercalation into '$TiOF_2$' proceeds via a two-step mechanism (at 1.8 and 1.2 V) after the first cycle. These ions may be intercalated into two different sites, each site with a broad energy domain. De-intercalation is also a two-step mechanism. In 'NbO_2F', Li^+ intercalation–de-intercalation is only a one-step process with a broad distribution of energy, or it may be two sites with overlapping energies, in the potential range, 1.4–1.8 V. This is characteristic of an amorphous material. In the case of crystalline cathode materials such as $LiCoO_2$ or $Li(Ni_{0.8}Co_{0.2})O_2$, it is noted that fairly sharp and well-defined CV peaks are encountered for the intercalation and de-intercalation of Li [2,3,30,35] and in these compounds crystal structure destruction does not eventuate.

3.4. Charge–discharge reaction mechanism

The galvanostatic discharge–charge and CV data for $TiOF_2$ and NbO_2F and the ex situ XRD studies on 'Li_xTiOF_2' described above show that crystal structure destruction takes place during the first discharge once the voltage is reduced to 0.8–0.9 V for $TiOF_2$ and 1.3–1.4 V for NbO_2F. During cycling, 1.52 mol of Li/Ti in 'Li_xTiOF_2' and 1.0 mol of Li/Nb in 'Li_xNbO_2F' are recycleable between 0.005 and 3.0 V. The discharge–charge mechanism can be inferred from the related studies carried out on the Mo containing compounds, $MnMoO_4$ [17], Na_xMoO_3 [15,16] and $CaMoO_4$ [32] and on binary metal fluorides/oxides reported by Li et al. [34]. In the case of Mo compounds, it was proposed that, upon deep discharge to 0.005 V versus Li, structure destruction occurs followed by the formation of an inert matrix, Li–A–O (A = Na, Ca or Mn), and an 'electrochemically active' amorphous oxide bronze, 'Li_xMoO_y', in which Mo adopts a zero or low-valency (1+ or 2+). During the charge operation (oxidation), Li^+ ions (and electrons) are released to give a phase, 'Li_nMoO_z'. Subsequent discharge–charge reactions involve the formation and decomposition of 'Li_xMoO_y' and contribute to the reversible capacity [15–17,32].

Evidence for a complex amorphous composite consisting of a 'Li_xMoO_y, $x>y$' in intimate contact with Li_2O was presented using Li NMR and X-ray absorption spectral data during lithium-cycling of the Li–$Na_{0.25}MoO_3$ system by Leroux et al. [15]. For the TiF_3/Li system, it was shown that a LiF/Ti 'amorphous mixture' formed during discharge and Li-extraction resulted in the formation of nano-crystalline TiF_3 [34]. In the present case, a similar mechanism may be operating in the amorphous composite, 'Li_xTi/NbO_y' with the LiF (formed during the first discharge) acting as an inert matrix and involving lower valency states of Ti($\leq$3+) and Nb($\leq$4+) during cycling. Formation of Ti or Nb metal particles can be ruled out during the first discharge or subsequent cycling since only 3.46 and 3.55 mol of Li are consumed per mole of $TiOF_2$ and NbO_2F, respectively, during the first discharge. Detailed microscopic in situ studies during cycling are required to establish the actual mechanism.

3.5. Electrochemical impedance spectroscopy

Impedance spectral studies (EIS) on electrode materials at various voltages during cycling provide information on surface film formation, factors governing the cycling stability such as charge-transfer resistance, bulk resistance and Li-ion kinetics. Extensive studies on various negative-electrode materials like graphite [35], SnO [36], $Li_4Ti_5O_{12}$ [6], $Ca_2Fe_2O_5$ and $Ca_2Co_2O_5$ [31] and $CaWO_4$ [33] have been reported. Studies have also been made on several oxide cathodes, e.g., $LiCoO_2$, $LiNiO_2$ [37–43]. In the present study, EIS measurements at room temperature have been conducted on cells with $TiOF_2$ or NbO_2F positive electrodes in order to understand the reasons for the observed differences in their cycleability. Spectra were recorded at select voltages between 0.005 and 3.0 V at a current of 30 mA g^{-1} during the first cycle. After the desired number of cycles, the cells were discharged to 0.005 V or charged to 3.0 V, relaxed for 3 h at the given voltage, and impedance spectra were measured. The Nyquist plots (Z' versus $-Z''$) for $TiOF_2$ and NbO_2F are shown in Figs. 6 and 7, respectively. The impedance spectra obtained during the first cycle for a given electrode at different states-of-discharge are given in Figs. 6a and 7a. Spectra obtained during the first cycle on electrodes at two different states-of-charge (1.0 and 3.0 V) are displayed in Figs. 6b and 7b. The spectra for fully discharged electrodes (0.005 V) after different discharge are given in Figs. 6c and 7c, while those obtained on fully charged electrodes (3.0 V) after different numbers of charge cycles are presented in Figs. 6d and 7d.

The impedance spectra were analyzed by fitting to an equivalent electrical circuit composed of: R_i (resistance); a constant phase element, CPE_i (due to the depressed semicircle observed in the spectra); a Warburg impedance (W_s); the intercalation capacitance (C_{int}). The circuit is shown in Fig. 8 and various subscripts are defined in the accompanying legend. This circuit conforms with the recent interpretation of the impedance spectra of cathode and anode materials reported in the literature [37,40,43,44]. The symbols in Figs. 6 and 7 are the experimental data, whereas the continuous lines are the fit to the circuit of Fig. 8. The data were also fitted using the slightly modified circuit employed by Nobili et al. [40,43]. The derived impedance parameters deviated trivially from those obtained using the circuit in Fig. 8. The resistance (impedance) due to the surface film, including the SEI formed on the electrode, is represented by R_{sf}. The parameter R_{ct} refers to the charge-transfer resistance to Li-ions at the interface between the electrode and electrolyte. The contribution R_b arises from the electronic resistivity of the active material and the ionic conductivity in the pores of the composite electrode (active material + conducting carbon + binder) filled with the electrolyte [44].

The ideal Warburg response, a straight line inclined at an angle of $\alpha = 45^\circ$ to the real axis (Z') in the complex impedance plane (Nyquist plot, Z' versus $-Z''$), is characteristic of Li-ion diffusion through the homogeneous single phase of the test electrode. Similarly, the ideal intercalation capacitance response is a

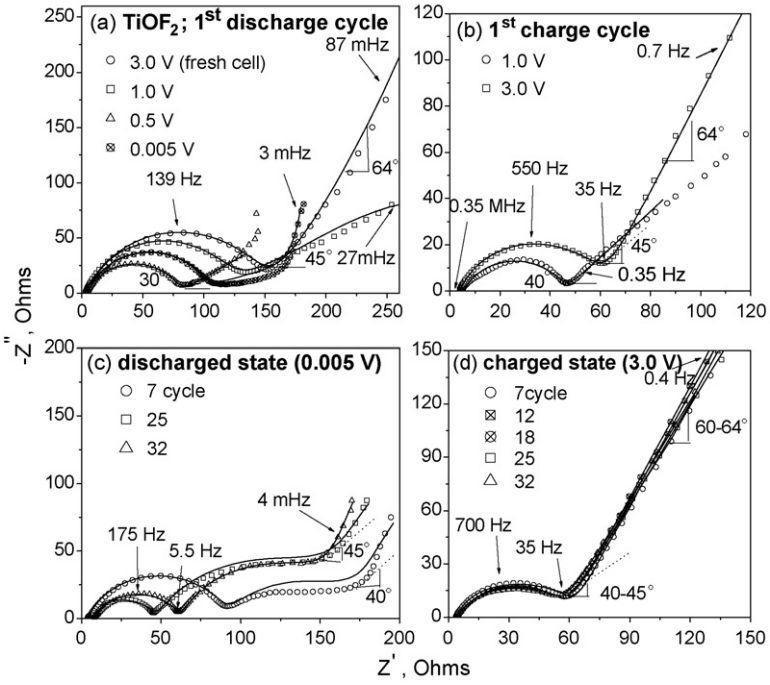

Fig. 6. Impedance spectra of $TiOF_2$ vs. Li: (a) at various voltages during first discharge, (b) at 1.0 and 3.0 V during first-charge cycle, (c) at 0.005 V at end of cycles 7, 25 and 32 and (d) at 3.0 V at end of cycles 7, 12, 18, 25 and 32. Voltages, frequencies, α and α' values at selected regions are shown. Symbols represent experimental data. Continuous lines represent fitting to equivalent circuit shown in Fig. 8 to extract impedance parameters. Geometric area of electrodes is 2 cm^2.

straight line perpendicular to the Z'-axis with $\alpha' = 90°$. Lower α and α' values are encountered in real systems depending on the nature of the active material, the existence of two-phase regions, inhomogeneities in the composite electrode, the impressed voltage and the number of cycles [41,45,46]. In this study, the α values range from 35° to 45° and α' values from 60° to 64° (Figs. 6 and 7). Since the changes occurring in the oxyfluoride electrode during cycling are greater than those at the counter (Li-metal) electrode, the variations in the impedance spectra and relevant parameters as a function of voltage can be safely

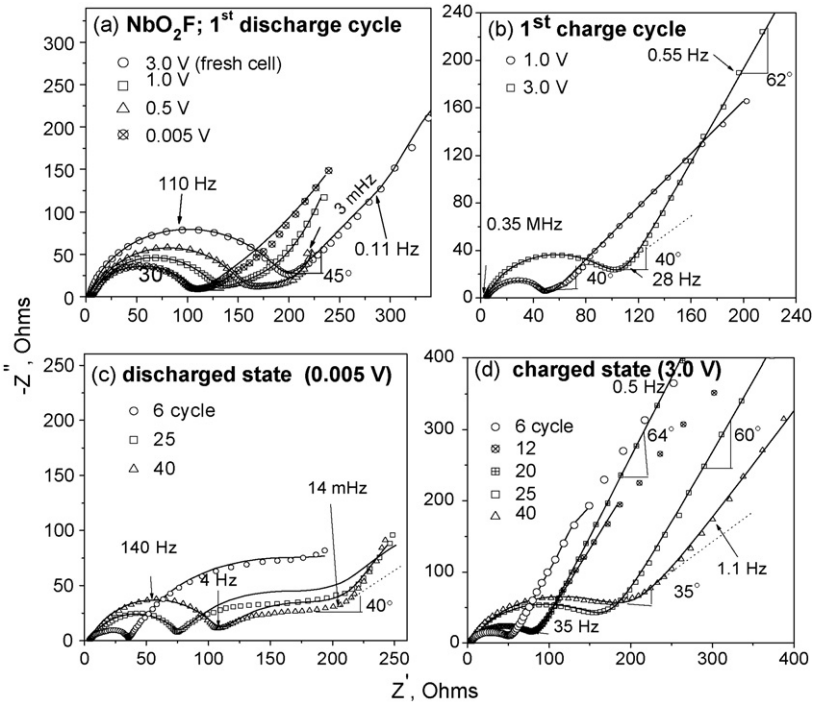

Fig. 7. Impedance spectra of NbO_2F vs. Li: (a) at various voltages during first discharge, (b) at 1.0 and 3.0 V during first-charge cycle, (c) at 0.005 V at end of cycles 6, 25 and 40 and (d) at 3.0 V at end of cycles 6, 12, 20, 25 and 40. Voltages, frequencies, α and α' values at selected regions are shown. Symbols represent experimental data. Continuous lines represent fitting to equivalent circuit shown in Fig. 8 to extract impedance parameters. Geometric area of electrodes is 2 cm^2.

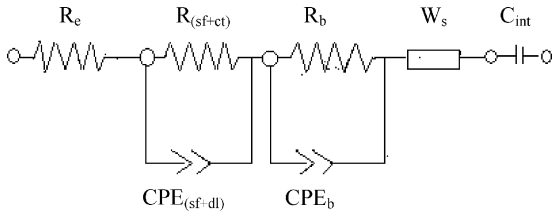

Fig. 8. Equivalent circuit used for fitting impedance spectra consisting R_i and $R_i||CPE_i$ combinations. R_e, $R_{(sf+ct)}$ and R_b are impedances (resistances) due to electrolyte and cell components, surface film (sf) plus charge transfer (ct) and bulk (b), respectively. CPE_i is the respective constant-phase element to account for depressed semicircle in experimental spectra (dl refers to double layer). W_s is the finite length Warburg (short-circuit terminus) element and C_{int} is the intercalation capacitance.

attributed to the test electrode of the two-electrode cell. The nominal surface area of the electrode is 2 cm^2 and the impedance parameters can be normalized whereever necessary.

A fresh cell of $TiOF_2$ versus Li with an OCV of ~3.0 V shows a single depressed semicircle in the high-frequency region (>0.14 kHz) that, after curve fitting, gives an impedance of 141 (±3) Ω. This is attributed to a combination of the surface film and the charge-transfer resistance ($R_{(sf+ct)}$). The associated $CPE_{(sf+dl)}$ is 30 (±5) μF. The semicircle is followed by Warburg-type behaviour in the low-frequency region ($\alpha = 45°$, 5.5–0.22 Hz). During the first discharge, the $R_{(sf+ct)}$ falls to <100 Ω at voltages of 1.0, 0.5 and 0.005 V. At 0.005 V, however, the spectrum shows a slightly sloping behaviour in the low-frequency region (<1 Hz). The act of development into a semicircle shows the onset of bulk impedance, R_b. During the first-charge cycle, at 1.0 and 3.0 V, a single depressed semicircle followed by the Warburg region ($\alpha = 40°$ and 45°, respectively) (<0.6 Hz) is observed (Fig. 6b), which indicates a contribution only from $R_{(sf+ct)}$. The fitted values of $R_{(sf+ct)}$ are 40 and 56 (±3) Ω at 1.0 and 3.0 V, respectively. These are smaller than those encountered at the respective voltages during the first-discharge cycle. The calculated $CPE_{(sf+dl)}$ value at 1.0 V is fairly large, viz., 108 (±5) μF, but drops to 34 (±5) μF at 3.0 V.

Spectra were collected in the fully discharged state at 0.005 V during cycles 7, 25 and 32 (Fig. 6c). As expected, the spectra are qualitatively different from those at the end of the first discharge, since the electrode process is now occurring in the amorphous composite, 'Li_xTiO_y'. The second depressed semicircle is now well-developed in the frequency range 4 Hz to 4 mHz and clearly delineates R_b from $R_{(sf+ct)}$. The fitted values of R_b are in the range 75–110 (±3) Ω, whereas the $R_{(sf+ct)}$ values fall in the range 42–86 (±3) Ω. The $CPE_{(sf+dl)}$ values are in the range 50–105 (±5) μF. The corresponding values of CPE_b range from 16 to 35 (±5) mF. These effective values of capacitance are in accord with expectation [44].

Spectra in the fully charged state (at 3.0 V) at the end of cycles 7, 12, 18, 25 and 32 are shown in Fig. 6d. Similar to the spectrum at the end of the first cycle (Fig. 6b), only one depressed semicircle is seen, followed by a Warburg region ($\alpha = 40–45°$) and an intercalation capacitance region ($\alpha' = 60–64°$). This indicates that the bulk resistance (R_b) is negligibly small in the charged state. Further, the spectra overlap well and the extracted $R_{(sf+ct)}$ (56 (±3) Ω) and $CPE_{(sf+dl)}$ (70 (±5) μF) remain constant irrespective of the cycle number. In addition, the $R_{(sf+ct)}$ values are almost the same as those found in the fully discharged state after the 25th cycle. Thus, very good lithium-recycleability of 'Li–$TiOF_2$' system is ensured due to the stable $R_{(sf+ct)}$ values, near zero R_b in the charged state, and $R_b < 110$ Ω in the fully discharged state. This shows that the amorphous composite, 'Li_xTiO_y' in the charged state is an excellent electronic conductor, due to the depleted lithium in it and the relatively larger amount of 'TiO_y', $y < 2$. Large changes in R_b values have also been encountered in cathode materials like $Li_{1-x}CoO_2$ [39] and $Li_{1-x}(Ni_{0.8}Co_{0.2})O_2$ [40], depending on the depth-of-charge (increasing x), and are attributed to reversible semiconductor–metal transformations during cycling.

The impedance spectra of NbO_2F versus Li resemble those of $TiOF_2$, but the values of the impedance parameters are different. The fresh cell with an OCV of about 3.0 V shows a single depressed semicircle with a fitted value of $R_{(sf+ct)} = 184$ (±3) Ω. The frequency at the maximum of Z'' is 110 Hz (Fig. 7a). The Warburg region ($\alpha = 45°$) occurs at low frequency, <0.2 Hz. During the first discharge at 1.0 and 0.5 V, the resistances are 109 and 97 (±3) Ω, respectively. The value of $R_{(sf+ct)}$ increases to 141 (±3) Ω at 0.005 V, the deep discharge limit. The spectrum at 0.005 V also shows a plateau before the onset of a Warburg-type region ($\alpha = 30°$) below 5 mHz, i.e., similar to that shown by $TiOF_2$ that indicates the onset of R_b, the bulk impedance. During the first charge, at 1.0 and 3.0 V, only one semicircle is seen followed by a Warburg region ($\alpha = 40°$; Fig. 7b). The respective $R_{(sf+ct)}$ values at 1.0 and 3.0 V are 43 and 99 (±3) Ω. The $CPE_{(sf+dl)}$ values are found to vary in the range 26–57 (±5) μF during the first cycle.

The spectra in the fully discharged state (at 0.005 V) for cycles 6, 25 and 40 are shown in Fig. 7c. Two semicircles followed by a Warburg region are clearly observed ($\alpha = 40–45°$) except for the sixth cycle. These were fitted to $R_{(sf+ct)}$ and R_b circuit elements. A clear trend can be seen in the variation of $R_{(sf+ct)}$ with increase in cycle number, from cycles 6 to 25 to 40, in that the value increases from 33 to 70 to 102 (±3) Ω whereas the R_b decreases from 183 to 103 to 90 (±5) Ω. The respective $CPE_{(sf+dl)}$ and CPE_b values are in the range 156–43 μF and 37–15 mF.

The spectra in the charged state (3.0 V) during cycles 6–40 resemble that of the first cycle, with one single semicircle followed by a Warburg region ($\alpha = 35°$) at low frequencies. This indicates that the R_b contribution is almost nil, similar to the case of the Li–$TiOF_2$ system (Figs. 6d and 7d). In the present case, however, the fitted values of $R_{(sf+ct)}$ increase with cycle number: 42 → 70 → 71 → 157 → 172 (±3) Ω for cycles 6, 12, 20, 25 and 40, respectively. The corresponding values of $CPE_{(sf+dl)}$ do not show any systematic variation and lie in the range 32–42 (±5) μF during cycles 6–40. The increase of $R_{(sf+ct)}$ with cycle number (6–40 cycles) should, in principle, be reflected as capacity fading in the Li–NbO_2F system, even though the galvanostatic cycling data show stable and reversible capacities (up to 40 cycles; Fig. 4b). Possibly, capacity fading may set in after 40 cycles, if the increasing trend of $R_{(sf+ct)}$ continues.

The resistance due to electrolyte and cell components (R_e) and C_{int} obtained by fitting the spectra ranges from 4 to 8

(±2) Ω and 0.15 to 2.7 (±0.1) F during the cycling of both the oxyfluorides. Bohnke et al. [28] reported impedance spectra and analysis during the first discharge (Li-insertion) up to $x = 1.65$ in Li_xNbO_2F and the present study is in general agreement with results of these authors, except that the values of $R_{(sf+ct)}$ are much smaller. It is noted that the impedance spectra and parameters of the Li–$TiOF_2$ and Li–NbO_2F systems are similar with minor variations and are consistent with the observed galvanostatic cycling data.

4. Summary and conclusions

Lithium insertion and extraction into/from the oxyfluorides $TiOF_2$ and NbO_2F, which possess the cubic structure, have been investigated by electrochemical methods. Crystal structure destruction occurs during the first-discharge reaction with Li at voltages below 0.8–0.9 V for Li_xTiOF_2 as shown by ex situ XRD, and for $V \leq 1.4$ V for Li_xNbO_2F. When first discharged to 0.005 V versus Li, the x values are 3.46 and 3.55 mol of Li per formula unit, respectively. The amorphous phases of Li_xTiOF_2/NbO_2F at this stage may consist of 'Li_x-Ti/Nb-O_y' oxide bronze (and LiF) with the transition metal ions in a low valence state. Lithium can be extracted from this bronze by charging to 3.0 V.

Galvanostatic charge–discharge cycling of 'Li_xTiO_y' in the range 0.005–3.0 V at a current density of 30 mA g^{-1} yields a capacity of 425 (±5) mAh g^{-1} that is stable during 5–50 cycles, whereas at 65 mA g^{-1} (*C*/6 rate) a capacity of 400 (±5) mAh g^{-1} during 5–100 cycles is obtained with no noticeable capacity fading. This value corresponds to 1.52 (±0.02) mol of recycleable Li/Ti. The coulombic efficiency (η) is >98% at both current densities. When cycled in the range 0.5–3.0 V at 60 mA g^{-1}, a lower capacity (280 mAh g^{-1} at the 10th cycle) is obtained, which degrades by ∼10% after 40 cycles. Results on 'Li_xNbO_y' show good reversibility of the electrode and a $\eta > 98\%$ is achieved after only 10 cycles (range 0.005–3.0 V at 30 mA g^{-1}; *C*/6 rate). The capacity of 180 (±5) mAh g^{-1} (0.97 ± 0.03 mol of Li/Nb) is stable up to 40 cycles. When cycled in the range 0.5–3.0 V at 15 mA g^{-1} or 1.0–3.0 V at 30 mA g^{-1}, lower capacities followed by slight capacity fading are observed up to 40 cycles. In both the 'Li_xTiO_y' and 'Li_xNbO_y' systems, the average discharge and charge voltages are 1.2–1.4 and 1.7–1.8 V, respectively. These values are comparable with those encountered in other prospective oxide anodes like CoO, NiO, $Ca_2Co_2O_5$, $CaMoO_4$ and in TiF_3. Ex situ XRD of the Li_xTiOF_2 electrode during the first cycle confirms destruction of the crystal structure. The observed CV data have been interpreted.

Impedance spectra have been measured on both oxyfluorides at various voltages during the first cycle, in both the fully discharged state (to 0.005 V) and the charged state (to 3.0 V) after a selected number of cycles. The data have been fitted to an equivalent circuit to extract the relevant parameters $R_{(sf+ct)}$ and R_b, as well as the associated CPEs. After six cycles, a contribution from the bulk resistance (R_b) is seen clearly in the spectra at 0.005 V in both compounds, whereas the R_b is almost zero in the fully charged state (3.0 V). After six cycles, the combined surface film and charge-transfer resistance ($R_{(sf+ct)}$) at 3.0 V remains constant at 56 (±3) Ω in the range 7–40 cycles for 'Li_xTiO_y', but it increases with cycle number in 'Li_xNbO_y' (42–172 (±3) Ω).

A reversible and stable capacity of 400 mAh g^{-1} up to 100 cycles is shown by 'Li_xTiO_y', which is higher than the theoretical capacity of graphite (372 mAh g^{-1}). Such behaviour, combined with the fact that Ti oxides are cheap, abundant and environmentally compatible, makes this oxyfluoride an attractive anode material for lithium-ion batteries.

Acknowledgement

Thanks are due to Mrs. N. Sharma, Department of Physics, NUS, for helpful discussions.

References

[1] J.-M. Tarascon, M. Armand, Nature 414 (2001) 359.
[2] W.A. Van Schalkwijk, B. Scrosati (Eds.), Advances in Lithium-Ion Batteries, Kluwer Academic/Plenum Publishers, USA, 2002.
[3] G.-A. Nazri, G. Pistoia (Eds.), Lithium Batteries: Science and Technology, Kluwer Academic Publishers, USA, 2003.
[4] E. Ferg, R.J. Gummow, A. de Kock, M.M. Thackeray, J. Electrochem. Soc. 14 (1994) L147.
[5] T. Ohzuku, A. Ueda, N. Yamamoto, J. Electrochem. Soc. 142 (1995) 1431.
[6] G.X. Wang, D.H. Bradhurst, S.X. Dou, H.K. Liu, J. Power Sources 83 (1999) 156.
[7] M. Winter, J.O. Besenhard, Electrochim. Acta 45 (1999) 31.
[8] Y. Idota, T. Kubota, A. Matsufuji, Y. Maekawa, T. Miyasaka, Science 276 (1997) 1395.
[9] I.A. Courtney, J.R. Dahn, J. Electrochem. Soc. 144 (1997) 2045.
[10] S. Machill, T. Shodai, Y. Sakurai, J.-I. Yamaki, J. Power Sources 73 (1998) 216.
[11] I.A. Courtney, W.R. McKinnon, J.R. Dahn, J. Electrochem. Soc. 146 (1999) 59.
[12] P. Poizot, S. Laruelle, S. Grugeon, L. Dupont, J.-M. Tarascon, Nature 407 (2000) 496.
[13] M.N. Obrovac, R.A. Dunlap, R.J. Sanderson, J.R. Dahn, J. Electrochem. Soc. 148 (2001) A576.
[14] G.X. Wang, Y. Chen, K. Konstantinov, M. Lindsay, H.K. Liu, S.X. Dou, J. Power Sources 109 (2002) 142.
[15] F. Leroux, G.R. Goward, W.P. Power, L.F. Nazar, Electrochem. Solid-State Lett. 1 (1998) 255.
[16] F. Leroux, L.F. Nazar, Solid State Ionics 133 (2000) 37.
[17] S.S. Kim, S. Ogura, H. Ikuta, Y. Uchimoto, M. Wakihara, Solid State Ionics 146 (2002) 249.
[18] P.A. Connor, J.T.S. Irvine, J. Power Sources 97/98 (2001) 223.
[19] M. Behm, J.T.S. Irvine, Electrochim. Acta 47 (2002) 1727.
[20] P.A. Connor, J.T.S. Irvine, Electrochim. Acta 47 (2002) 2885.
[21] N. Sharma, K.M. Shaju, G.V. Subba Rao, B.V.R. Chowdari, Electrochem. Commun. 4 (2002) 947.
[22] N. Sharma, K.M. Shaju, G.V. Subba Rao, B.V.R. Chowdari, J. Power Sources 139 (2005) 250.
[23] K. Vorres, J. Donohue, Acta Crystallogr. 8 (1955) 25.
[24] S. Carlson, A.K. Larsson, F.E. Rohrer, Acta Crystallogr. B56 (2000) 189.
[25] D.W. Murphy, M. Greenblatt, R.J. Cava, S.M. Zahurak, Solid State Ionics 5 (1981) 327.
[26] L. Permer, M. Lundberg, J. Solid State Chem. 81 (1989) 21.
[27] C. Bohnke, O. Bohnke, J.L. Fourquet, Mol. Cryst. Liq. Cryst. 311 (1998) 23.
[28] C. Bohnke, J.L. Fourquet, N. Randrianantoandro, T. Brousse, O. Crosnier, J. Solid State Electrochem. 5 (2001) 1.
[29] S. Madhavi, Ph.D. Thesis, National University of Singapore, Singapore, 2002.

[30] K.S. Tan, M.V. Reddy, G.V. Subba Rao, B.V.R. Chowdari, J. Power Sources 141 (2005) 129.
[31] N. Sharma, K.M. Shaju, G.V. Subba Rao, B.V.R. Chowdari, Electrochim. Acta 49 (2004) 1035.
[32] N. Sharma, K.M. Shaju, G.V. Subba Rao, B.V.R. Chowdari, Chem. Mater. 16 (2004) 504.
[33] N. Sharma, G.V. Subba Rao, B.V.R. Chowdari, Electrochim. Acta 50 (2005) 5305.
[34] H. Li, P. Balaya, J. Maier, J. Electrochem. Soc. 151 (2004) A1878.
[35] D. Aurbach, B. Markovsky, I. Weissman, E. Levi, Y. Ein-Eli, Electrochim. Acta 45 (1999) 67.
[36] D. Aurbach, A. Nimberger, B. Markovsky, E. Levi, E. Sominski, A. Gedanken, Chem. Mater. 14 (2002) 4155.
[37] F. Croce, F. Nobili, A. Deptula, W. Landa, R. Tossici, A. D'Epifanio, B. Scrosati, R. Marassi, Electrochem. Commun. 1 (1999) 605.
[38] M.D. Levi, K. Gamolsky, D. Aurbach, U. Heider, R. Oesten, Electrochim. Acta 45 (2000) 1781.
[39] D. Aurbach, M.D. Levi, E. Levi, H. Teller, B. Markovsky, G. Salitra, U. Heider, L. Heider, J. Electrochem. Soc. 145 (1998) 3024.
[40] F. Nobili, F. Croce, B. Scrosati, R. Marassi, Chem. Mater. 13 (2001) 1642.
[41] K.M. Shaju, G.V. Subba Rao, B.V.R. Chowdari, J. Electrochem. Soc. 151 (2004) A1324.
[42] K.M. Shaju, G.V. Subba Rao, B.V.R. Chowdari, Electrochim. Acta 49 (2004) 1565.
[43] F. Nobili, S. Dsoke, F. Croce, R. Marassi, Electrochim. Acta 50 (2005) 2307.
[44] M.D. Levi, D. Aurbach, J. Phys. Chem. B 108 (2004) 11693.
[45] Y.-M. Choi, S.-I. Pyun, Solid State Ionics 99 (1997) 173.
[46] Z. Lu, M.D. Levi, G. Salitra, Y. Gofer, E. Levi, D. Aurbach, J. Electroanal. Chem. 491 (2000) 211.